Interfacial Water Molecules as Agents for Phase Change Control and Proton Conductivity Enhancement in the Ammonium Vanadyl Tartrate System

*Marko Dunatov,[a] Krešimir Molčanov,[a] Zoran Štefanić,[a] Robert Kruk,[b] and Lidija Androš Dubraja[a]**

[a]*Ruđer Bošković Institute, Bijenička cesta 54, 10000 Zagreb, Croatia*

[b]*Institute of Nanotechnology, Karlsruhe Institute of Technology, Hermann-von-Helmholtz-Platz 1, 76344, Eggenstein-Leopoldshafen, Germany*

KEYWORDS

vanadium, L-tartaric acid, proton conductivity, impedance spectroscopy, interfacial water, phase transformation, charge density, in situ ATR-FTIR

ABSTRACT

This study demonstrates the reversible structural transformation, single crystal-to-single crystal, of the ammonium vanadyl (*L*-tartrate) complex salt from the hydrate phase to the anhydrous phase. The transformation can be initiated by stimuli such as temperature, humidity, or vacuum conditions. The hydrate and anhydrous phases exhibit a tetragonal structure ($P4_12_12$), with marked differences in hydrogen bonding due to the presence or absence of one water molecule per asymmetric unit. The intricate relationship between crystal packing and intermolecular interactions in the hydrate phase was investigated by crystallographic charge density analysis revealing, at the molecular level, the reasons for the observed five orders of magnitude higher proton conductivity of the hydrate phase compared to the anhydrous phase. To gain further insight into the processes occurring at the surfaces of grain boundaries and the proton transfer mechanisms in this system, rehydration of the complex salt was carried out using D_2O instead of H_2O and monitored by *in situ* ATR-FTIR spectroscopy. The results highlight the critical role of interfacial water molecules in driving structural transformations and influencing proton conductivity.

INTRODUCTION

The incorporation of multidentate ligands into the coordination sphere of metals is a well-known strategy for producing highly stable and structurally tunable supramolecular assemblies achieved through various noncovalent interactions between the desired molecular building blocks, inorganic anions, and other constituent units.[1,2] The use of naturally occurring substances in crystal engineering is a very convenient way to introduce flexibility into these crystalline solid-state products.[3] However, the aforementioned flexibility in structure is in some cases the limiting factor when it comes to the stability of such compounds, i.e., they undergo various chemical or structural transformations depending on the environmental conditions and external stimuli, even if these stimuli mean only a slight change in temperature or humidity.[4-8] On the other hand, from an application point of view, stimuli-responsiveness can be a very valuable property for the development of new devices and technologies.[9,10] In this sense, it is very important to optimize and test the conditions under which a particular structural transformation occurs and to establish the correct structure-property correlation. Since metal-organic compounds are usually produced under milder conditions compared to metal oxides, i.e., less energy is consumed, and the mass fraction of metals, which are often expensive and scarce, is much lower, and they can be more easily recovered or recycled, they could be considered in the coming years as an environmentally friendly and sustainable alternative to the materials currently used in devices.

Recently, solid-state proton conductors in purely organic and inorganic as well as hybrid metal-organic systems have attracted considerable attention because of their potential use in fuel cells for alternative energy production.[11-15] One of the best proton-conducting materials contains Keggin-type acidic polyoxometalate units that can efficiently transport protons since the effective surface charge density is low due to the spreading of the negative charge over the exterior surface

oxygens.[16,17] The disadvantage of these systems, however, is the clear reliance of proton conductivity on the level of hydration, and also the low thermal stability of such systems.[18] Additionally, the amount of hydration in these solids influences the mechanism of proton transport, ranging from Grotthuss for the pseudoanhydrous or completely anhydrous state to vehicular for a high number of water molecules.[19] The activation energy of charge transport, E_a, which is on the order of a few 0.1 eV in the case of Grotthuss-like proton transfer through extended hydrogen bonds, can be used to determine whether the first or second mechanism predominates. The change in the proton conductivity of a system under certain stimuli can be the result of either intrinsic factors, such as structural or compositional changes, or interfacial effects, i.e. by interplay of protonic species at the interfaces (grain boundaries and surfaces). Hydrated surfaces, or layers of water adhered to the solid surfaces that are in equilibrium with the vapor phase, are unavoidable when preparing or testing the material under atmospheric conditions.[20,21] It has been shown that water coats almost all surfaces, even insulators, under ambient conditions.[22,23] Apart from effecting the properties of a system, adsorbed water layers can built up certain chemical potential and induce a structural changes in a material.

We have recently reported that a complex salt composed of tetraethylammonium cations and oxovanadium(V) complex anions undergoes multiple structural transformations, triggered by changes in environmental conditions (relative humidity, temperature).[6] Under humid conditions the complex salt accommodates a large number of water molecules in the structure, leading to remarkable increase in volume of unit cell (10^3 Å^3), accompanied with enhancement of conductivity.[6] To further on test the potential of simpler metal-oxo anions in the design of efficient proton conductors, we have chosen to study a complex salt composed of ammonium cations and bis[(*L*-tartrato)oxovanadium(IV)] anions. The preparation of the hydrate phase, $(NH_4)_4[V_2O_2($*L*-

tart)$_2$]·2H$_2$O [*L*-tart = fully deprotonated *L*-tartaric acid, $(C_4O_6H_2)^{4-}$], was first described by Conn[24] in 1963, starting from the reduction of metavanadate with hydrazine and subsequent complexation with *L*-tartaric acid. According to the studies conducted, the hydrate phase transforms into an anhydrous phase under different stimuli and rehydrates reversibly at high humidity. Crystallographic charge density analysis of the hydrate phase was conducted to study possible charge transfer effects between donor and acceptor molecules connected by hydrogen bonds. Structural properties and crystal transformations were correlated with electrical properties studied by impedance spectroscopy. Our studies show that interfacial water molecules, which assemble in layers on surface of grain boundaries, are acting as agents for phase change control and moreover enhance the proton conductivity in the ammonium vanadyl (*L*-tartrate) complex salt.

EXPERIMENTAL SECTION

Starting Materials. *L*-(+)-tartaric acid was purchased from Alfa Aesar. Glacial acetic acid, hydrazine hydrate, ammonium hydroxide solution and ammonium metavanadate were purchased from Sigma Aldrich.

$(NH_4)_4[V_2O_2(L\text{-tart})_2]\cdot 2H_2O$. The hydrate phase was synthesized according to literature procedure,[24] which was slightly modified. A reaction mixture containing glacial acetic acid (0.36 mL), water (0.64 mL) and hydrazine hydrate (0.03 mL, 55 wt. %) was stirred and heated at 65 °C. Ammonium metavanadate (0.117 g, 1 mmol) was added gradually over a period of 5 minutes. After 10 minutes, evolution of nitrogen ceased and ammonium metavanadate dissolved giving a blue solution. *L*-(+)-tartaric acid (0.150 g, 1 mmol) was then added to the reaction mixture under constant stirring and heating. After 5 minutes concentrated ammonia solution (1.2 mL) was added to the reaction mixture, and the color of the solution changed from blue to violet. The pH of the final solution was 8. The resulting solution was transferred to a beaker and violet prism crystals of

$(NH_4)_4[V_2O_2(tart)_2]\cdot 2H_2O$ crystallized overnight. The crystals were filtered off. The yield was 0.22 g (82%). The addition of ethanol (1 mL) to the solution can promote crystallization giving smaller crystals, but the yield is almost stoichiometric.

Physical Measurements. Attenuated total reflectance Fourier transform infrared (ATR-FTIR) spectra were recorded in the 4000–400 cm^{-1} range using a Perkin-Elmer FT-IR Frontier spectrometer. Humidity-dependent ATR-FTIR measurements were recorded *in situ* in the chamber with a manual device (HH414, Omega Engineering, Inc.) for monitoring the relative humidity (RH) that was attached to the ATR module of the spectrometer. The RH value was adjusted in two ways: *i*) in dynamic experiments by mixing dry N_2 and wet air (see Scheme 1 in Supporting Information); *ii*) in static experiments by exposure to D_2O, or saturated aqueous solutions of NaBr (RH 60%) and NaCl (RH 75%) salts. Thermal analysis (TG/DTA) was performed using a Shimadzu DTG-60H analyzer, in the range from room temperature to 1073 K, in a stream of synthetic air at a heating rate of 10 K min^{-1}. Differential scanning calorimetry (DSC) thermograms were recorded using Netzsch DSC 214 Polyma calorimeter, calibrated with adamantane, In, Sn, Bi, Zn and CsCl standards and operating in a dynamic mode. Two heating and cooling cycles at temperatures ranging from 293 to 433 K in an extra pure nitrogen environment were performed at a rate of 5 K min^{-1}. The electrical properties were studied by impedance spectroscopy using an impedance analyzer (PalmSens4) in the frequency range from 10 Hz to 1 MHz in a custom-made insulating chamber. A thermoelectric Peltier module was placed on one side of the chamber to provide the required heating and cooling, and the sample was placed on it. The temperature was controlled with the TEC-1091-NTC-PIN controller. Additional thermocouple probe was placed above the sample for extra temperature monitoring. Specific RH value in the custom-made chamber was achieved by exposure to saturated aqueous solutions of different salts (LiCl, NaBr

and NaCl) and in vacuum (100 mbar). For measurements the polycrystalline sample was pressed (estimated by ca. 8 GPa) into a cylindrical pellet with a diameter of 5 mm and a thickness of 0.5 mm having a 3.5 mm diameter sputter coated Au electrodes on the opposite surfaces of the pellet. The impedance spectra were analyzed by equivalent circuit modeling using the non-linear least-squares fitting procedure.

Crystallography. The single-crystal X-ray diffraction data were collected by ω-scans using Cu-Kα radiation (λ = 1.54179 Å, microfocus tube, mirror monochromator) on a Rigaku XtaLAB Synergy diffractometer at 100 and 298 K. The crystal data, experimental conditions and final refinement parameters are summarized in Table S1 in Supporting Information. Data reduction, including multiscan absorption correction, was performed with the CrysAlisPRO software package. Molecular and crystal structures were solved by direct methods using the program SIR2019[25] and spherical refinement was performed using the full-matrix least-squares method based on F^2 with anisotropic displacement parameters for all non-hydrogen atoms (SHELXL-2014/7).[26] Both programs were operating under the WinGX program package.[27] The hydrogen atoms attached to the C atoms of the tartrate anions were treated as riding in idealized positions, with the C–H distances of 0.93 Å and displacement parameters assigned as $U_{iso}(H) = 1.2U_{eq}(C)$. The hydrogen atoms of water molecules were identified based on difference Fourier maps where [O–H distances were restrained to a target value of 0.85(2) Å, and the H–O–H angle to 104°].

Diffraction data for the charge density study were collected using Mo-Kα radiation up to the maximum resolution of 0.5 Å and the multiple integrated reflections were averaged for the corresponding space groups using the program SORTAV[28] adapted to area detector data. Multipolar refinement was carried out vs. all reflections F^2 with program package MoPro[29] using reflections up to s = 1.0 $Å^{-1}$. In later phases of refinement the resolution was reduced to s = 0.9 $Å^{-}$

[1]. The O, N and C atoms were modelled as octupoles and hydrogens as dipoles; loose restraints were used for multipoles and kappas of chemically equivalent atoms. Due to an approximate twofold symmetry of $[V_2O_2(L\text{-tart})_2]^{4-}$ anion, multipoles of the V1 atom were restrained to a C_2 symmetry, while O atoms and C1 and C4 from tartrate anions were restrained to planarity. N atoms of the ammonium cations were restrained to tetrahedral symmetry and water atom O8 to C_{2v} symmetry. C–H bond lengths were restrained to 1.099(5) Å, C–N to 1.036(5) and O–H to 0.983(5) Å. Topological bond orders were calculated using the formula[30]: $n_{topo} = a + b\,\lambda_3 + c\,(\lambda_1 + \lambda_2) + d\,\rho_{cp}$. Coefficients *a*, *b*, *c* and *d* were taken from the literature: for C–C bonds $a = -0.522$, $b = -1.695$, $c = 0.00$, $d = 8.473$;[31] for C–H and C–N bonds $a = -0.153$, $b = 0.481$, $c = 0.983$, $d = 8.087$;[32] for C–O bonds $a = 0.776$, $b = 0.267$, $c = 0$, $d = 0$.[31] Geometrical calculations were carried out with PLATON[33] and the figures were generated using ORTEP,[27] CCDC-Mercury[34] and MoPRO Viewer[35]. Charge density calculations were carried out using the program package MoPRO[29].

The powder X-ray diffraction data (PXRD) were collected in reflection mode with Cu-Kα radiation (λ = 1.54060 Å) on a Malvern Panalytical Empyrean diffractometer using a step size of 0.001° in the 2θ range between 5° and 60°. Temperature modulated measurements were performed *in situ* in a high temperature oven chamber, and RH modulated measurements were performed *ex situ*. The crystal structures of hydrate and anhydrous phases were used as a structural model for Rietveld refinement of powder data from polycrystalline samples and gave a satisfactory fit (Figures S8 and S9 in Supporting Information).

RESULTS AND DISCUSSION

The structure of $(NH_4)_4[V_2O_2(tart)_2]\cdot 2H_2O$ has been reported over 50 years ago by Forrest and Prout,[36] who were the first to structurally characterize and confirm the existence of dimeric vanadyl tartrate ions, which attracted considerable attention at the time because of the difficulties in

preparation and the complex (pH-dependent) solution behavior of various vanadium tartrate species. The compound crystallizes in the space groups $P4_12_12$ with the asymmetric unit consisting of two crystalographically independent NH_4^+ cations, one half of the vanadyl tartrate dimer anion lying on a double two-fold axis, and one water molecule of crystallization (Figure 1a). The hydrate phase exhibits an extended 3D hydrogen bonding geometry involving all constituent units. Each oxygen atom of the fully deprotonated *L*-tartrate ligands serves as a proton acceptor. In addition, there are several 1D hydrogen bonding chains between ammonium cations and water molecules that are parallel to the *a* and *b* axes (Figure 2a).

The high-resolution diffraction study of $(NH_4)_4[V_2O_2(tart)_2]\cdot 2H_2O$ was undertaken to reveal fine details in hydrogen bonding which may provide an explanation of conductivity. In addition, it is interesting for study, since only a couple of vanadium compounds have been studied by quantum crystallography.[37,38] The molecular charges calculated from refined valence populations (P_{val}) are −3.95 for the $[V_2O_2(tart)_2]^{4-}$, +0.93 and +0.91 for two respective ammonium cations (N1 and N2) and +0.13 for the water molecule O8. These values are in a good agreement with the formal charges. The coordination sphere of the vanadium cation involves a short vanadyl bond V1=O1, 1.6274(18) Å and four longer bonds with hydroxyl O atoms, ranging from 1.9064(14) to 2.0216(13) Å. These two types of bonds are qualitatively different, as can be seen in the maps of deformation density (Figures 1b and S1) and Laplacian (Figures 1c and S2). The V1=O1 bond, with a maximum electron density at the critical point of 1.732 e $Å^{-3}$ (Table S2) is clearly covalent, while the other four bonds are of a dominantly ionic character (maximum electron densities in the critical points are 0.553 - 0.655 e $Å^{-3}$ (Table S2) and are more similar to coordination bonds in previously studied Cu(II) and Mn(II) complexes.[39–42]

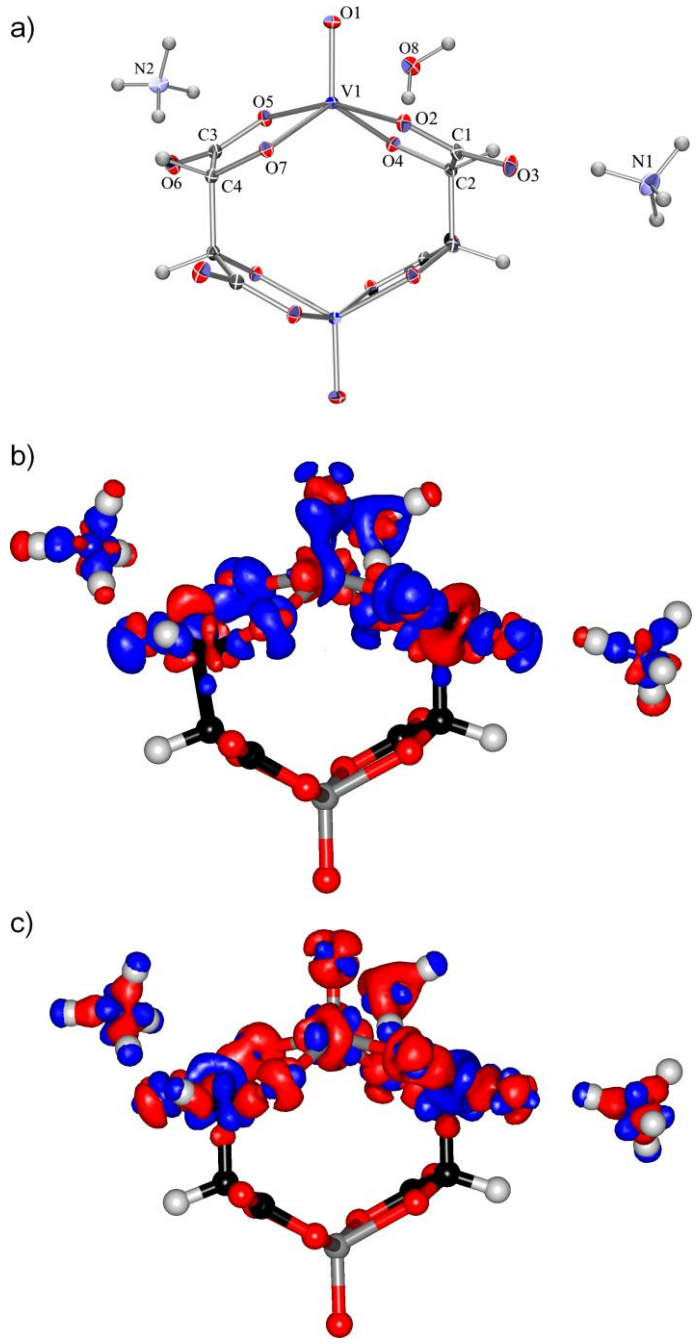

Figure 1. Crystal structure and charge density of $(NH_4)_4[V_2O_2(tart)_2]\cdot 2H_2O$: a) ORTEP-3 drawing with atom numbering scheme, displacement ellipsoids drawn for the probability of 50 % and hydrogen atoms shown as spheres of arbitrary radii; b) isosurface of 3D deformation density for ±0.1 e $Å^{-3}$ (blue is positive and red is negative); and c) isosurface of 3D Laplacian for ±5 e $Å^{-3}$ (blue is positive and red is negative).

The geometry and topology of the electron density of the tartrate ligands are as expected. There are a total of 14 symmetry-independent hydrogen bonds in the crystal packing, ten N–H···O, two O–H···O and two weaker C–H···O (Table S3). According to geometries and electron densities (Table S4) they can be classified as medium strong or weak therefore, no proton transfer is expected.[44] Two hydrogen bonds which form the chains (see description above), N1–H2N···O8 and N1–H3N···O8 are also typical medium strong hydrogen bonds[45] with respective maximum electron densities at the critical points of 0.231 and 0.158 e $Å^{-3}$. Deformation density (Figure S1) and Laplacian of electron density (Figure S2) are in agreement with this; there are no features in residual density (Figures S3 and S4) which would suggest a possible proton disorder as a result of proton transfer.

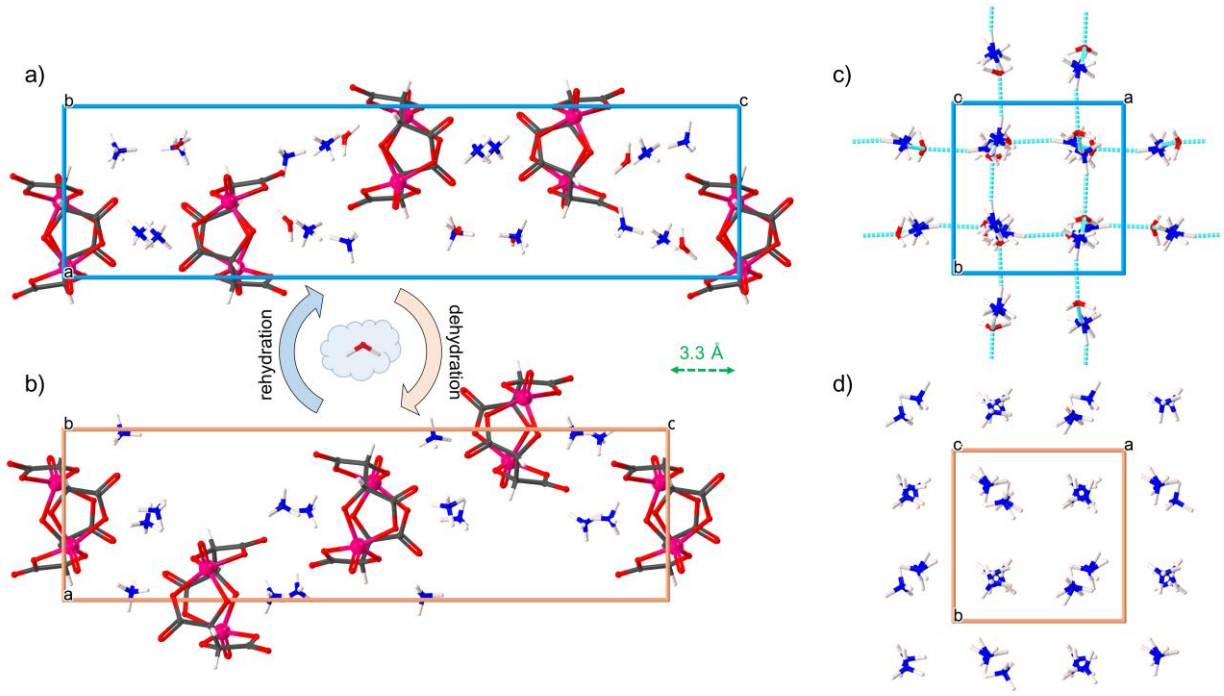

Figure 2. Comparison between crystal packings of: a) hydrate phase; b) anhydrous phase viewed along the *b* axis. Packing viewed along the *c* axis of: c) ammonium cations and water molecules

in the hydrate phase; d) ammonium cations in the anhydrous phase. Cyan sticks represent the hydrogen bonding between ammonium cations and water molecules.

The hydrate phase $(NH_4)_4[V_2O_2(tart)_2]\cdot 2H_2O$ undergoes dehydration process to a anhydrous phase $(NH_4)_4[V_2O_2(tart)_2]$ that can be triggered by different stimuli: temperature or relative humidity (RH). The transformation occurs if hydrate phase is: *i*) evacuated in low vacuum (~0.1 mbar); *ii*) heated to 373 K; or *iii*) exposed to dry nitrogen gas (RH < 5%). Figure 3 shows PXRD patterns after sample manipulation under different stimuli, inducing corresponding structural changes. The transformation from the hydrate to the anhydrous phase belongs to a single-crystal-to-single-crystal type transition, which was confirmed by single-crystal XRD measurements. The structure of the anhydrous phase is tetragonal $P4_12_12$. The loss of the water molecule during dehydration causes a shortening of the *c*-axis by 3.3 Å (see Figure 2; Table 1). The crystal symmetry remains intact during this transformation, so that the *a*- and *b*-axes remain unchanged. Figure 3 shows that 004 reflections are shifted to higher 2θ values during the structural transformations, indicating a shortening of the *c*-axis. In the anhydrous form, the ammonium cations interact with their surrounding vanadyl tartrate anions, more specifically with the oxygen proton acceptors, via even shorter hydrogen bonds. However, the 1D hydrogen bonding chain consisting only of ammonium cations and water molecules is lost (Figure 2c and d).

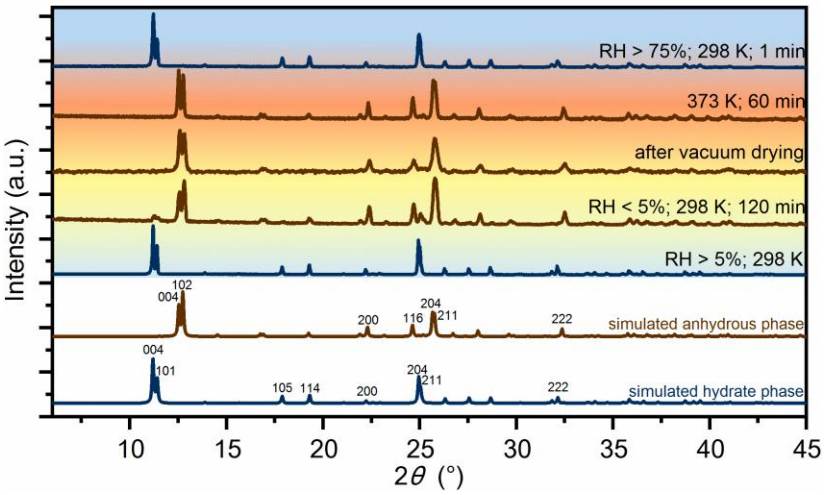

Figure 3. PXRD patterns following the structural transformation from hydrate to anhydrous phase under different stimuli. Simulated diffractograms from single-crystal XRD data are given for comparison.

Table 1. Unit cell parameters and space group of the hydrate and anhydrous phases of ammonium vanadyl(*L*-tartrate).

PHASE	HYDRATE	ANHYDROUS
T / K	298	298
Mr/ g mol^{-1}	267.10	249.08
Space group	$P4_12_12$	$P4_12_12$
a / Å	7.9910(1)	7.9688(3)
b / Å	7.9910(1)	7.9688(3)
c / Å	31.5460(7)	28.2233(14)
$\alpha = \beta = \gamma$ / °	90	90
Z	8	8
ρ_{calcd}/g cm^{-3}	1.761	1.846
V / Å^3	2014.40(7)	1792.23(16)

Additional insight into the changes caused by dehydration and the dynamics of the process can be studied *in situ* by ATR-FTIR spectroscopy (Figures 4, S10–S15). The observation of changes in the stretching vibration frequencies of the N–H, C–O, V–O and V=O bonds is clearly visible.

There are two crystalographically independent ammonium cations in the asymmetric unit, and consequently the N–H stretching vibrations differ. The N–H stretching vibrations of the ammonium cation that forms a hydrogen bonding chain with the water molecule in the hydrate phase appear at 3185 and 2980 cm^{-1} and shift to 3169 and 3050 cm^{-1}, respectively, during dehydration, while the vibrations of the second ammonium cation are not affected by hydration/dehydration and appear as bands at 2899 and 2834 cm^{-1} (Figure S10 in Supporting Information).[46] The most significant change concerns the most intense band in the spectra associated with the stretching vibration of the terminal V=O bond.[47,48] During dehydration, this band is blue-shifted from 940 to 959 cm^{-1}, and according to structural analysis the bond itself is elongated from 1.622 to 1.636 Å.

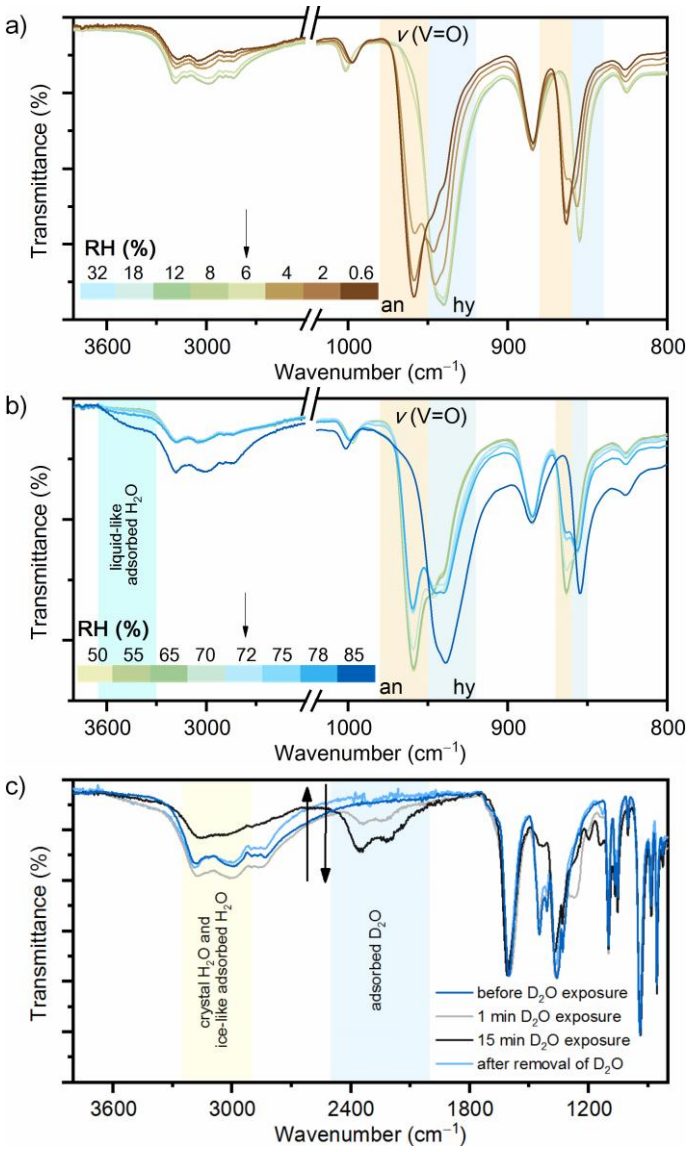

Figure 4. *In situ* humidity-dependent ATR-FTIR spectra following transformation: *a*) from hydrate phase to anhydrous phase; *b*) from anhydrous phase to hydrate phase, *c*) during exposure to D_2O of hydrate phase.

IR spectroscopy is very valuable to examine the dynamics of the phase transition associated with dehydration/rehydration. According to *in situ* ATR-FTIR spectroscopy (Figure 4a), the anhydrous phase begins to appear at RH ~6% at 298 K. When the anhydrous phase is fully converted, it remains stable up to RH ~70% and begins to convert to the hydrate phase as RH increases further

(Figure S11 in Supporting Information). Along with the recovery of the hydrate phase at RH 75%, a new broad band appears in the spectra at 3400 cm^{-1} corresponding to the O–H stretching vibration of the water molecules adsorbed on the surface of the grain boundaries. A small peak at 3740 cm^{-1} is also detectable for the high RH values, corresponding to the O–H stretching of water molecules that do not have enough nearest neighbors to saturate the hydrogen bonding. According to previous studies by Kim[49]and Norby[50], there are three types of adsorbed water molecules: molecular adsorbed water and a hydrogen-bonded layer as part of the so-called *ice-like* layer and a more loosely bound *liquid-like* layer that appears at RH >60%. The *ice-like* layer is observed as a broad peak centered at 3200 cm^{-1}, and studies of silicon oxide surfaces have shown that it is present even at RH below 30%.[51] In the spectra of both the hydrate and anhydrous phases, the region around 3200 cm^{-1} is overlapped with more intense N–H and O–H stretching vibrations coming from ammonium cations and crystal water molecules. Since ATR-FTIR spectra in low vacuum still show broad O–H vibrations centered at 3200 cm^{-1}, this is an indication that first layer of water molecules part of the *ice-like* layer is forming a strong interaction via hydrogen bonds to the surface. More loosely bound water layers, part of the so-called *liquid-like* adsorbed water, are characterized by a peak at 3400 cm^{-1}.[49] According to studies from IR on ammonium vanadyl (*L*-tartrate) compound, the appearance of a peak at 3365 cm^{-1} associated with a *liquid-like* adsorbed water layer precedes the formation of the hydrate phase from the anhydrous one. During the 240-minute exposure at RH 60%, the structural transformation is not detected, and after 10 minutes at RH 75%, there is an indication of the formation of the hydrate phase (Figure 4b). Scheme 1 presents the humidity-dependent structural transformation in simplified form. For example, both the anhydrous and hydrate phases can be stable at 50% RH, but they do not appear as mixed phases (Scheme 1). In a sense, the compound has a memory effect depending on whether it was previously

dried or exposed to high RH. Only at the transition values of RH (5% and 75%) there are mixed phases. Once formed, a *liquid-like* adsorbed water layer is difficult to remove, which also indicates that strong hydrogen bonds exist between these molecules (see Figures S12, S13 and S15 in the Supporting Information).

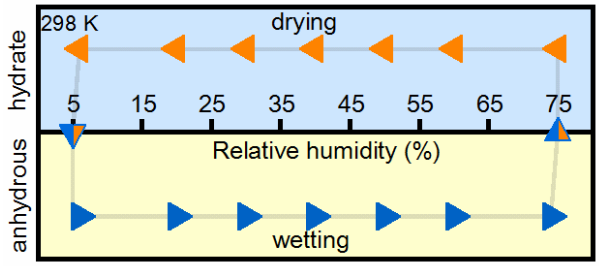

Scheme 1. Humidity-dependent transformation in the ammonium vanadyl tartrate system.

ATR-FTIR spectroscopy was also used to follow the reversible exchange reaction of H_2O for D_2O both *in-situ* and *ex-situ* to further confirm the existence of water layers on the surface of the studied complex salt. After exposing the sample to the D_2O-air atmosphere the intensity of the bands associated with the O–H stretching vibration [ν(O–H)] of the *ice-like* layer water molecules (a broad peak centered at 3200 cm^{-1}) immediately starts to decrease, while two broad bands associated with the O–D stretching vibrations appear at 2385 and 2207 cm^{-1} (Figure 4c). Similar observation was also found during exposure of nano-structured yttria-doped zirconia to D_2O-air atmosphere.[52] The O–H stretching vibrations coming from water molecules of crystallization remain in the spectra, because these molecules are less likely to be exchanged with D_2O due to stronger interactions. Other changes in the spectra are associated with small shifts of the vibrations coming from bis[(*L*-tartrato)oxovanadium(IV)] anions, namely ν_{as}(CO), ν_s(CO), ν_{as}(V=O) and ν_s(V=O), that are located at the surface and that form O–D···O bonds with newly formed D_2O layers. Surface analysis performed in Mercury's CSD-Particle module[34] gives an insight on electrostatic potential of particular crystal surfaces in studied complex salt. This analysis shows,

for example, that planes (004), (204), and (101) are rich in hydrogen accepting or donating groups (red and blue areas in Scheme 2, also in Figure S7). Such surfaces have a high tendency to form hydrogen bonds with water molecules from the vapor phase, and the formation of water layers is expected, as schematically shown in Scheme 2. When D_2O is introduced into the system, the adsorbed (both *ice-like* and *liquid-like*) H_2O layers rapidly exchange with it, consistent with theoretical and experimental evidence showing that D_2O shifts the equilibrium between inter-residue hydrogen bonds and competing D_2O/H_2O solvents in its favor.[53] Accordingly, removal of D_2O and exposure to air at RH 38% results in full recovery of the initial spectrum (light blue line in Figure 4c).

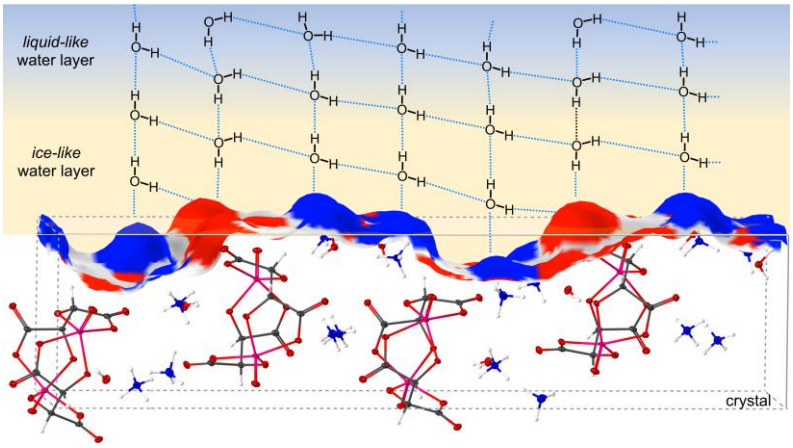

Scheme 2. Surface analysis of the (101) plane in the hydrate phase having hydrogen bonding acceptor (red area) and donor (blue area) groups.

TG/DTA analysis (Figure S16) shows that the process of elimination of water of crystallization for the hydrate phase is finished at 400 K. The anhydrous phase is further on stable up to 500 K. Differential scanning calorimetry (Figure 5) revealed significant differences in the enthalpies associated with water release from the anhydrous phase, the hydrate phase and the hydrate phase in wet conditions. This observation is fully consistent with ATR-FTIR measurements that show presence of water layers even for anhydrous phase, whose number is further on increasing in wet

conditions in the hydrate phase. Under atmospheric conditions all samples have hydrated surfaces, and therefore the measured heat effect related to water release is the sum of the heat coming from the intrinsic water of crystallization and the heat content due to interfacial effects.[54] For the anhydrous phase, the measured heat effect is the sum of the heat content related to water release from the surface and grain boundaries. Noticeable difference between the enthalpies measured for the hydrated phase under dry and wet conditions is a clear sign of multiple water layers that are bound to the surface and grain boundaries when RH is above 75%. These structured water layers are shown schematically in Scheme 2. From the values of enthalpies, the number of *ice-like* water layers present in the anhydrous phase and the hydrate phase under dry conditions is approximately equal to the number of *liquid-like* water layers in the hydrate phase under wet conditions.

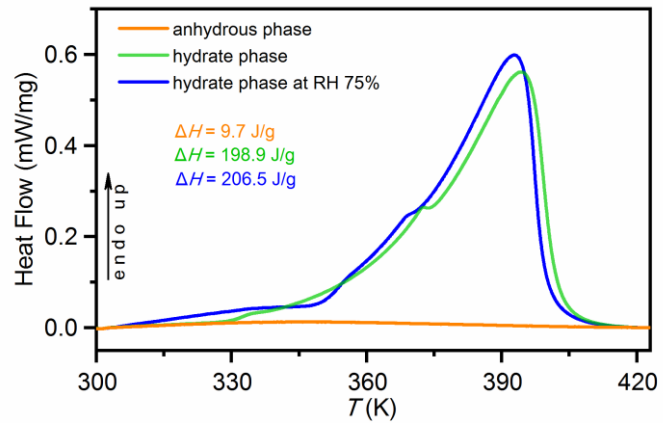

Figure 5. DSC curves of the anhydrous and hydrate phases in dry conditions, and the hydrate phase in wet conditions measured at a heating rate of 5 K min^{-1}.

The proton conductivities of the hydrate and anhydrous phases were investigated by AC impedance spectroscopy, using pressed pellets of the powder sample with two gold electrodes sputtered onto the surface. The measurement was performed in the following sequence: first, the anhydrous phase was measured in vacuum and at RH 20%; then, the anhydrous phase was

converted to the hydrate phase by exposing it to a saturated aqueous NaCl solution (RH 75%) for 12 hours and measuring it; then, the hydrate phase was exposed to RH 20–30% for 12 hours and then to a saturated aqueous NaBr solution (RH 60%) for 12 hours, after which the measurement was performed at RH 60%. This sequence of sample manipulations achieved complete conversion between the anhydrous and hydrate phases and equilibrium between the solid/gas interfaces at different RH. The dependence of conductivity (σ) on RH is non-linear (Figure 6a), reflecting the sequence of structural transformations under different conditions. Figures 6b and 6c show Nyquist plots for the anhydrous phase measured in an evacuated chamber (pressure around 100 mbar) and at RH 20%, respectively. The corresponding Nyquist plots can be described by an equivalent circuit consisting of a resistor (R) and a constant phase element (CPE) connected in parallel (Figure S17, Supporting Information). The conductivity of the anhydrous phase at room temperature (298 K) and low vacuum pressure was calculated to be of 3.66×10^{-9} S cm^{-1}. When the anhydrous phase is measured at 20% RH, the conductivity increases to 1.14×10^{-8} S cm^{-1}, not due to intrinsic factors, but because of the formation of additional *ice-like* water layers on the surface and at the grain boundaries, which contribute to the overall conductivity. This is also confirmed by ATR-FTIR spectra of the anhydrous phase in vacuum and RH 20%, where differences are observed in the spectral region indicative of the adsorbed *ice-like* water layers (see Figure S14 in the Supporting Information). Previous spectroscopic studies have also shown that up to three monolayers of *ice-like* adsorbed water can form at less than 30% RH.[49]

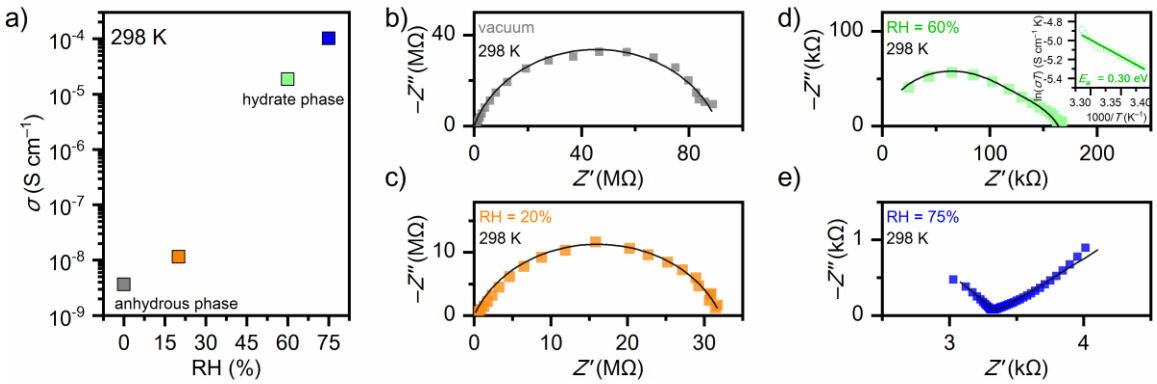

Figure 6. a) Plot of conductivity *vs* relative humidity at 298 K, following structural transformation from hydrate phase at high RH and anhydrous phase at low RH; b)–e) Complex impedance plane (Nyquist plot) recorded at different RH at 298 K with fitted arcs (solid lines). Inset at d) the ln(σT) *vs* T^{-1} plot with Arrhenius fit as solid line.

According to the *in situ* ATR-FTIR studies, the anhydrous phase begins to convert to a hydrate phase when RH reaches 75%. After conversion of the sample pellet to the hydrate phase by exposure to air at RH 75% for a sufficient time (typically 12 hours), the conductivity increases by a factor of 10^5 to 1.01×10^{-4} S cm^{-1}, as shown by the data from the impedance plot (Figure 6e, Figure S17). The conversion of the anhydrous to the hydrate phase is accompanied by the formation of a *liquid-like* layer of adsorbed water at the interfaces (grain boundaries and surfaces). This suggests that two different factors are responsible for the observed increase in hydrate phase conductivity at RH 75%: *i*) crystal water molecules in the structure *via* 1D hydrogen bonding chains that serve as proton conduction pathways (see Figure 2c); *ii*) adsorbed *liquid-like* water layers. To determine the actual contribution of the crystal water molecules to the overall increase in conductivity, the sample pellet was exposed to dry conditions for 12 hours (RH 20–30%), and after the *liquid-like* layers were removed, the AC impedance measurements were performed at RH 60%. Reducing RH to 60% and removing the so-called *liquid-like* layer causes the hydrate phase conductivity to decrease to a value of 1.88×10^{-5} S cm^{-1} at 298 K. This is a clear indication that

the conductivity of the hydrate phase is strongly influenced by the formation of the *liquid-like* layer of adsorbed water at the surface and grain boundaries, which happens when RH is 75% or higher. According to the *in situ* ATR-FTIR measurements, *liquid-like* layer of adsorbed water appears when RH reaches ~75% (Figure S12 in Supporting Information), and there is a large hysteresis in the wetting and drying process mostly due to the stability of these *liquid-like* layers. Since the phase transition from anhydrous to hydrate phase occurs only at RH above 75%, it is very likely that the formation of the so-called *liquid-like* layer is a prerequisite for the phase transition. In other words, its absence at RH 60% during the wetting process, as demonstrated by ATR-FTIR, is the reason for the stability of the anhydrous phase at such high RH (see Figure S11 in the Supporting Information).

Furthermore, the thermal dependencies of the conductivity for the hydrate phase conditioned at 60% RH were investigated. The activation energies (E_a) were calculated based on the linear fit to Arrhenius plots [$\ln(\sigma T)$ *vs* 1000 T^{-1}] (inset in Figure 6d, all data given in Figure S18, Supporting Information). The E_a values of 0.30 eV at 60% RH are typical for proton-conducting materials and comparable to the activation energy for reference materials, e.g., Nafion (E_a < 0.4 eV)[19] and other related materials.[55,56] Considering the crystal structure of the hydrate phase, supported by charge density studies, and the exact position of water molecules in the structures, the Grotthuss mechanism is more likely compared to the vehicle mechanism. The large difference between the conductivities of the anhydrous and hydrate phases is also related to their structural properties, i.e., the geometry of the hydrogen bonds. In the hydrate phase, the H_2O molecules are arranged together with the NH_4^+ cations through hydrogen bonds to form infinite chains running along the *a* and *b* axes (Figure 2c), which allow more efficient proton hopping, compared to the anhydrous phase, where the loss of the water molecule disrupts these proton conduction pathways (Figure 2d). The

effect of the adsorbed water on conductivity is also detectable in both the anhydrous and hydrate phases, consistent with *in situ* ATR-FTIR measurements showing the presence of *ice-like* and *liquid-like* adsorbed water layers occurring at different RH levels.

CONCLUSIONS

This work presents the structural and electrical study of an ammonium vanadyl-(*L*-tartrate) complex salt, which undergoes reversible single-crystal-to-single-crystal transformations during dehydration/rehydration processes induced by variations in relative humidity and temperature. Structural transformations of the hydrate phase to the anhydrous phase and vice versa are followed by *in situ* and *ex situ* XRD and ATR-FTIR measurements, providing insight into the structural features responsible for electrical properties such as proton conductivity. In this complex salt the soft crystal packing of constituting units, different from the one in e.g. porous ceramics or metal-organic frameworks and coordination polymers, is responsible for the observed proton transport properties and performance. The loss of the water molecule in anhydrous phase causes a shortening of the *c*-axis by 3.3 Å without changing the symmetry. In addition, the 1D hydrogen bonding chains between the ammonium cations and the water molecules are lost in the anhydrous form, reflecting in drop of proton conductivity by three orders of magnitude, from 1.88×10^{-5} to 1.14×10^{-8} S cm^{-1}. Proton conduction is affected not only by changes in crystal structure, but also by the presence of tightly bound water molecules at grain boundaries, which are abundant in proton acceptors. Under humid condition (RH 75%) the generation of so called *liquid-like* layers of adsorbed water leads to one order of magnitude increase in proton conductivity, reaching the favorable value of 1.01×10^{-4} S cm^{-1}. Furthermore, the presence of tightly bound water molecules serves a dual purpose by both enhancing proton conduction and facilitating structural transformations. It can be seen that these water layers play a crucial role in the transition between

the anhydrous and hydrated phases, allowing conversion in both directions. In summary, our results show that the proton conductivity in the metal-organic complex salt can be attributed to two main sources: the protons present within the crystal structure and the water present at the surface and grain boundaries. These conduction pathways can be controlled by environmental conditions such as temperature and relative humidity.

ASSOCIATED CONTENT

Supporting Information. The Supporting Information is available free of charge.

X-ray crystallographic parameters, charge density analysis, ATR-FTIR spectra, TG/DTA and EIS data (PDF).

CCDC 2282760 and 2282761 contain the supplementary crystallographic data for this paper. These data can be obtained free of charge via www.ccdc.cam.ac.uk/data_request/cif, or by emailing data_request@ccdc.cam.ac.uk, or by contacting The Cambridge Crystallographic Data Centre, 12 Union Road, Cambridge CB2 1EZ, UK; fax: +44 1223 336033.

AUTHOR INFORMATION

Corresponding Author

*** Dr. Lidija Androš Dubraja**

Ruđer Bošković Institute

Bijenička cesta 54

10000 Zagreb, Croatia

Phone: +385 1 456 1184

E-mail: Lidija.Andros@irb.hr

Funding Sources

This work has been funded and supported by the Croatian Science Foundation Project No. UIP-2019-04-7433.

Notes

The authors declare no competing financial interest.

ACKNOWLEDGMENT

Financial support from the Croatian Science Foundation (UIP-2019-04-7433) and mobility Croatian-German (MZO-DAAD) bilateral project is gratefully acknowledged.

REFERENCES

(1) Yoshinari, N.; Konno, T. Multitopic Metal–Organic Carboxylates Available as Supramolecular Building Units. *Coord. Chem. Rev.* **2023**, *474*, 214850.

(2) Caruso, T.; De Luca, O.; Melfi, N.; Policicchio, A.; Pisarra, M.; Godbert, N.; Aiello, I.; Giorno, E.; Pacilè, D.; Moras, P.; Martín, F.; Rudolf, P.; Agostino, R. G.; Papagno, M.. Nearly-Freestanding Supramolecular Assembly with Tunable Structural Properties. *Sci. Rep.* **2023**, *13*, 2068.

(3) Miyata, M.; Shibakami, M.; Chirachanchai, S.; Takemoto, K.; Kasai, N.; Miki K. Guest-Responsive Structural Changes in Cholic Acid Intercalation Crystals. *Nature* **1990**, *343*, 446–447.

(4) Kato, M.; Ito, H.; Hasegawa, M.; Ishii, K. Soft Crystals: Flexible Response Systems with High Structural Order. *Chem. – Eur. J.* **2019**, *25*, 5105–5112.

(5) Ferreira da Rosa, P. P.; Kitagawa, Y.; Shoji, S.; Oyama, H.; Imaeda, K.; Nakayama, N.; Fushimi, K.; Uekusa, H.; Ueno, K.; Goto, H.; Hasegawa, Y. Preparation of Photonic Molecular Trains via Soft-Crystal Polymerization of Lanthanide Complexes. *Nat. Commun*. **2022**, *13*, 3660.

(6) Dunatov, M.; Puškarić, A.; Androš Dubraja, L. Multi-Stimuli Responsive (L-tartrato)oxovanadium(V) Complex Salt with Ferroelectric Switching and Thermistor Properties. *J. Mater. Chem. C* **2023**, *11*, 2880–2888.

(7) Li, B.; Duan, X.; Cheng, D.; Chen, X.; Gao, Z.; Ren, W.; Shao, K.-Z.; Zang, H.-Y. Controllable Transition Metal-Directed Assembly of $[Mo_2O_2S_2]^{2+}$ Building Blocks into Smart Molecular Humidity-Responsive Actuators. *J. Am. Chem. Soc*. **2023**, *145*, 4, 2243–2251.

(8) Dunatov, M.; Puškarić, A.; Pavić, L.; Štefanić, Z.; Androš Dubraja, L. Electrically Responsive Structural Transformations Triggered by Vapour and Temperature in a Series of Pleochroic Bis(oxalato)chromium(iii) Complex Salts. *J. Mater. Chem. C* **2022**, *10*, 8024–8033.

(9) Yan, D.; Wang, Z.; Zhang, Z. Stimuli-Responsive Crystalline Smart Materials: From Rational Design and Fabrication to Applications. *Acc. Chem. Res.* **2022**, *55*, 7, 1047–1058.

(10) Dong, J.; Wee, V.; Zhao, D. Stimuli-Responsive Metal–Organic Frameworks Enabled by Intrinsic Molecular Motion. *Nat. Mater.* **2022**, *21*, 1334–1340.

(11) Sadakiyo, M.; Yamada, T.; Honda, K.; Matsui, H.; Kitagawa H. Control of Crystalline Proton-Conducting Pathways by Water-Induced Transformations of Hydrogen-Bonding Networks in a Metal–Organic Framework. *J. Am. Chem. Soc*. **2014**, *136*, 21, 7701–7707.

(12) Lim, D.-W.; Sadakiyo, M.; Kitagawa, H. Proton Transfer in Hydrogen-Bonded Degenerate Systems of Water and Ammonia in Metal–Organic Frameworks. *Chem. Sci*. **2019**, *10*, 16–33.

(13) Stub, S. Ø.; Vøllestad, E.; Norby, T. Protonic Surface Conduction Controlled by Space Charge of Intersecting Grain Boundaries in Porous Ceramics. *J. Mater. Chem. A* **2018**, *6*, 8265–8270.

(14) Wang, H.; Wu, Q.; Ding, X.; Shao, Z.; Xu, W.; Zhao, Y., Xie, Q.; Meng, X.; Hou, H. The 50-Fold Enhanced Proton Conductivity Brought by Aqueous-Phase Single-Crystal-to-Single-Crystal Central Metal Exchange. *Inorg. Chem*. **2020**, *59*, 12, 8361–8368.

(15) Celik, E.; Ma, Y.; Brezesinski, T.; Elm, M. T. Ordered Mesoporous Metal Oxides for Electrochemical Applications: Correlation Between Structure, Electrical Properties and Device Performance. *Phys. Chem. Chem. Phys*. **2021**, *23*, 10706–10735.

(16) Nakamura, O.; Kodama, T.; Ogino, I.; Miyake, Y. High-Conductivity Solid Proton Conductrors: Dodecamolybdophosphoric Acid and DodecaTungstophosphoric Acid Crystals. *Chem. Lett.* **1979**, *8*, 17−18.

(17) Iwano, T.; Miyazawa, S.; Osuga, R.; Kondo, J. N.; Honjo, K.; Kitao, T.; Uemura, T.; Uchida, S. Confinement of Poly(allylamine) in Preyssler-Type Polyoxometalate and Potassium Ion Framework for Enhanced Proton Conductivity. *Commun. Chem*. **2019**, *2*, 9.

(18) Martinelli, A.; Otero-Mato, J. M.; Garaga, M. N.; Elamin, K.; Habibur Rahman, S. M.; Zwanziger, J. W.; Werner-Zwanziger, U.; Varela, L. M. A New Solid-State Proton Conductor:

The Salt Hydrate Based on Imidazolium and 12-Tungstophosphate. *J. Am. Chem. Soc*. **2021**, *143*, 13895−13907.

(19) Zhao, G.; Zhao, H.; Zhuang, X.; Shi, L.; Cheng, B.; Xu, X.; Yin, Y. Nanofiber Hybrid Membranes: Progress and Application in Proton Exchange Membranes. *J. Mater. Chem. A* **2021**, *9*, 3729−3766.

(20) Ewing, G. E. Thin Film Water. *J. Phys. Chem. B* **2004**, *108*, 41, 15953–15961.

(21) Hong, Y.-J.; Tai, L.-A.; Chen, H.-J.; Chang, P.; Yang, C.-S.; Yew, T.-R. Stable Water Layers on Solid Surfaces. *Phys. Chem. Chem. Phys.* **2016**, *18*, 5905–5909.

(22) Xu, J.-L.; Gowen, A. A. Time Series Fourier Transform Infrared Spectroscopy for Characterization of Water Vapor Sorption in Hydrophilic and Hydrophobic Polymeric Films. *Spectrochim. Acta A: Molecular and Biomolecular Spectroscopy* **2021***, 250*, 119371.

(23) Ewing, G. E. Ambient Thin Film Water on Insulator Surfaces. *Chem. Rev.* **2006**, *106*, 4, 1511–1526.

(24) Conn, G. J. B. U.S. Pat 3076830, *Chem. Abstr*. **1963**, *58*, 12375.

(25) Burla, M. C.; Caliandro, R.; Carrozzini, B.; Cascarano, G. L.; Cuocci, C.; Giacovazzo, C.; Mallamo, M.; Mazzone, A.; Polidori, G. Crystal Structure Determination and Refinement via SIR2014. *J. Appl. Crystallogr.* **2015**, *48*, 306–309.

(26) Sheldrick, G. M. Crystal Structure Refinement with SHELXL. *Acta Crystallogr., Sect. C: Struct. Chem.* **2015**, *C71*, 3−8.

(27) Farrugia, L. J. WinGX and ORTEP for Windows: An Update. *J. Appl. Crystallogr*. **2012**, *45*, 849−854.

(28) Blessing, R. H. Data Reduction and Error Analysis for Accurate Single Crystal Diffraction Intensities. *Crystallogr. Rev.* **1987**, *1*, 3−58.

(29) Jelsch, C.; Guillot, B.; Lagoutte, A.; Lecomte, C. *J.* Advances in Protein and Small-Molecule Charge-Density Refinement Methods Using MoPro. *Appl. Crystallogr*., **2005**, *38*, 38−54.

(30) Zarychta, B.; Zaleski, Z.; Kyzioł, J.; Dazskiewicz, Z.; Jelsch, C. Charge-Density Analysis of 1-nitroindoline: Refinement Quality Using Free R Factors and Restraints. *Acta Cryst. B.* **2011**, *B67*, 250−262.

(31) Howard, S. T.; Lamarche, O. Description of Covalent Bond Orders Using the Charge Density Topology. *J. Phys. Org. Chem*. **2003**, *16*, 133−141.

(32) Zhurova, E. A.; Zhurov, V. V.; Pinkerton, A. A. Structure and Bonding in β-HMX-Characterization of a Trans-Annular N···N Interaction. *J. Am. Chem. Soc*. **2007**, *129*, 13887−13893.

(33) Spek, A. L. Structure Validation in Chemical Crystallography. *Acta Crystallogr., Sect. D: Biol. Crystallogr.* **2009**, *D65*, 148−155.

(34) Macrae, F.; Edgington, P. R.; McCabe, P.; Pidcock, E.; Shields, G. P.; Taylor, R.; Towler, M.; van de Streek, J. Mercury: Visualization and Analysis of Crystal Structures. *J. Appl. Crystallogr.* **2006**, *39*, 453−457.

(35) Guillot, B. MoProViewer: a Molecule Viewer for the MoPro Charge-Density Analysis Program. *Acta Crystallogr. A.* **2012**, *68*, s204.

(36) Forrest, J. G.; Prout, C. K. The Crystal and Molecular Structure of Ammonium Vanadyl (+)-tartrate Monohydrate. *J . Chem. Soc. (A)* **1967**, 1312–1317.

(37) Terlan, B.; Borrmann, H.; Baranov, A.; Börnert, C.; Wagner, F. R.; Grin, Y. X-ray Charge-Density Analysis of Vanadium Diboride: a Comparison of Experiment and Theory. *Acta Crystallogr. A* **2010**, *A66*, s94.

(38) Xu, X.; Spasojević-De Bire, A.; Ghermani, N. E.; Wei, Y.; Novaković, S.; Bošnjaković-Pavlović, N.; Wu, P. Experimental Evidence of Charge Transfer in a Functionalized Hexavanadate: a High Resolution X-ray Diffraction Study. *Phys. Chem. Chem. Phys*. **2017**, *19*, 18162–18166.

(39) Vuković, V.; Molčanov, K.; Jelsch, C.; Wenger, E.; Krawczuk, A.; Jurić, M.; Androš Dubraja, L.; Kojić-Prodić, B. Malleable Electronic Structure of Chloranilic Acid and Its Species Determined by X-ray Charge Density Studies. *Cryst. Growth Des.* **2019**, *19*, 2802–2810.

(40) Chuang, Y.-C.; Sheu, C.-F.; Lee, G.-H.; Chen, Y.-S.; Wang, Y. Charge Density Studies of 3d Metal (Ni/Cu) Complexes with a Non-innocent Ligand. *Acta Crystallogr. B* **2017**, *B73*, 634–642.

(41) Farrugia, L. J.; Mallinson, P. R.; Stewart, B. Experimental Charge Density in the Transition Metal Complex $Mn_2(CO)_{10}$: a Comparative Study. Erratum. *Acta Crystallogr. B* **2003**, *B59*, 234–247.

(42) Wang, Y. Charge Density Analysis and Bond Characterization of 3d-Transition Metal Complexes. *J. Chin. Chem. Soc.* **2014**, *61*, 27–38.

(43) Pillet, S.; Souhassou, M.; Mathoniere, C.; Lecomte, C. Electron Density Distribution of an Oxamato Bridged Mn(II)−Cu(II) Bimetallic Chain and Correlation to Magnetic Properties. *J. Am. Chem. Soc.* **2004**, *126*, 1219–1228.

(44) Steiner, T. The Hydrogen Bond in the Solid State. *Angew. Chem., Int. Ed.* **2002**, *41*, 48–76.

(45) Molčanov, K.; Jelsch, C.; Wenger, E.; Stare, J.; Madsen, A. Ø.; Kojić-Prodić, B. Experimental Evidence of a 3-Centre, 2-Electron Covalent Bond Character of the Central O–H–O Fragment on the Zundel Cation in Crystals of Zundel Nitranilate Tetrahydrate. *CrystEngComm* **2017**, *19*, 3898–3901.

(46) Pankewitz, T.; Lagutschenkov, A.; Niedner-Schatteburg, G.; Xantheas, S. S.; Lee, Y.-T. Infrared Spectrum of NH_4^+ (H_2O): Evidence for Mode Specific Fragmentation. *J. Chem. Phys.* **2007**, *126*, 074307.

(47) Garcia-Jaca, J.; Insausti, M.; Cortes, R.; Rojo, T.; Pizarro, J. L.; Arriortua, M. I. A New Perspective of Vanadyl-tartrate Dimers. Synthesis, Crystal Structure, Spectroscopic and Magnetic Properties of the Chain Compound: $\{[BaVO(C_4H_2O_6)(H_2O)_4]_2\}]_{;n}$. *Polyhedron* **1994**, *13*, 357–364.

(48) Cao, J.; Xiong, Y.; Luo, X.; Chen, L.; Shi, J.; Zhou, M.; Xu, Y. A Pair of New Chiral Polyoxovanadates with Decent NLO Properties. *Dalton Trans*. **2018**, *47*, 6054–6058.

(49) Asay, D. B.; Kim, S. H. Evolution of the Adsorbed Water Layer Structure on Silicon Oxide at Room Temperature. *J. Phys. Chem*. B **2005**, *109*, 35, 16760–16763.

(50) Stub, S. Ø.; Vøllestad, E.; Norby, T. Mechanisms of Protonic Surface Transport in Porous Oxides: Example of YSZ. *J. Phys. Chem. C* **2017**, *121*, 23, 12817–12825.

(51) Du, Q.; Freysz, E.; Shen, Y. R. Surface Vibrational Spectroscopic Studies of Hydrogen Bonding and Hydrophobicity. *Science* **1994**, *264*, 826–828.

(52) Miyoshi, S.; Akao, Y.; Kuwata, N.; Kawamura, J.; Oyama, Y.; Yagi, T.; Yamaguchi, S. Low-Temperature Protonic Conduction Based on Surface Protonics: An Example of Nanostructured Yttria-Doped Zirconia. *Chem. Mater*. **2014**, *26*, 5194–5200.

(53) Clark, T.; Heske, J.; Kühne, T. D. Opposing Electronic and Nuclear Quantum Effects on Hydrogen Bonds in H_2O and D_2O. *ChemPhysChem* **2019**, *20*, 2461–2465.

(54) Radha, A. V.; Bomati-Miguel, O.; Ushakov, S. V.; Navrotsky, A.; Tartaj, P. Surface Enthalpy, Enthalpy of Water Adsorption, and Phase Stability in Nanocrystalline Monoclinic Zirconia. *J. Amer. Chem. Soc.* **2009**, *92*, 133–140.

(55) Yamada, T.; Nankawa, T. High Proton Conductivity of Zinc Oxalate Coordination Polymers Mediated by a Hydrogen Bond with Pyridinium. *Inorg. Chem*. **2016**, *55*, 17, 8267–8270.

(56) Maity, D. K.; Ghosh, S.; Otake, K.; Kitagawa, H.; Ghoshal, D. Proton Conductivity and Sorption Study in Three Sulfonic Group Functionalized Mixed Ligand Coordination Polymers and the Impact of Structural Dynamicity on Their Property. *Inorg. Chem.* **2019**, *58*, 19, 12943–12953.

TABLE OF CONTENTS SYNOPSIS

The presence of tightly bound and structured water molecules serves a dual purpose by both enhancing proton conduction and facilitating structural transformations in ammonium vanadyl (*L*-tartrate) complex salt.